

1 **Improvement of Soil Properties Maps using an Iterative Residual Correction Method**

2 Chengcheng Xu<sup>1</sup>, Elia Scudiero<sup>23</sup>, Ray Anderson<sup>32</sup>, Nathaniel Chaney<sup>1</sup>

3 <sup>1</sup> Department of Civil and Environmental Engineering, Duke University, Durham, NC 27705,

4 USA

5 <sup>2</sup> Department of Environmental Sciences, University of California Riverside, Riverside, CA

6 92521, USA

7 <sup>3</sup> United States Department of Agriculture – Agricultural Research Service, George E. Brown

8 Jr. Salinity Laboratory, Agricultural Water Efficiency and Salinity Research Unit, Riverside,

9 CA 92507, USA

10 *Correspondence to:* Chengcheng Xu (Chengcheng.xu@duke.edu)

11

12 **Short Summary**

13 Accurate soil information is vital. This study developed a method to improve existing  
14 probabilistic soil maps — spatially continuous maps providing prior estimates — by  
15 correcting their probability distributions as new soil data emerges. By iteratively adjusting  
16 previous predictions, the method increases both accuracy and certainty of soil maps. Its  
17 application in California enhanced predictions for several soil properties. This method can  
18 be further used for more soil properties and regions.

19

20 **Abstract**

21 Accurate mapping of soil properties is vital for many applications, yet existing models for  
22 digital soil maps often underestimate their spatial variability or prediction uncertainties,

23 which introduces risk for applications such as irrigation and drainage management. This  
24 study introduces an approach — iterative residual correction (IRC) — to update existing  
25 probabilistic soil maps when new soil observations become available. We demonstrated  
26 its application for enhanced soil mapping performance using a Californian case study. To  
27 implement this, we first generate prior probabilistic soil property maps using a pruned  
28 hierarchical Random Forest (pHRF) method. These prior estimates are then refined by  
29 integrating additional soil profile data and iteratively adjusting residuals of distribution of  
30 soil properties (reducing differences between observations and prior predictions) pixel by  
31 pixel. For this purpose, we employed Random Forest regressors to gradually adjust the soil  
32 property distributions and incrementally correct prior bias. Updated soil maps were  
33 evaluated over California and at 1-km resolution to test the methodology, using additional  
34 soil observations from the World Soil Information Service, the Soil Characterization  
35 Database, the University of California Riverside, and the United States Department of  
36 Agriculture Agricultural Research Service. Posterior soil texture predictions achieved an  
37 RMSE below 10, a 7% ~~relative reduction in errors (mass fraction of the fine-earth fraction)~~  
38 over priors. RMSE and spatial representation for soil organic matter and bulk density also  
39 improved. Furthermore, the method reduced prediction uncertainties (narrower prediction  
40 intervals compared to the priors) and enforced physical constraints on soil property  
41 bounds. Looking forward, this IRC method offers a scalable pathway to improve existing  
42 probabilistic soil maps, providing a strategy for the evolution of digital soil products as new  
43 soil observations emerge.

Deleted: %,

46 **1 Introduction**

47 Soils play an important role in regulating Earth’s water, energy, and nutrient cycles  
48 (Vereecken et al., 2016). Soil maps guide agricultural practices, ecosystem management,  
49 hydraulic modeling, and climate studies, such as crop modeling, flood risk assessment,  
50 groundwater management, and climate change (Vereecken et al., 2022). The importance  
51 of soil maps has increased with the advent of precision agriculture, including site-specific  
52 seeding, irrigation, and fertilization recommendations that intrinsically depend on high-  
53 resolution soil properties (Jiang et al., 2011; Li et al., 2019; Mueller et al., 2001; Ortuani et  
54 al., 2016). However, the accuracy and reliability of these management actions heavily  
55 depend on the quality of soil maps as a critical decision-making input. Traditional soil  
56 surveys involve field observations, laboratory analyses, and expert interpretation, but are  
57 labor-intensive and expensive (Grunwald et al., 2011; Rossiter et al., 2022; Soil Survey Staff  
58 et al., 2023). These limitations have driven the development of digital soil mapping (DSM)  
59 techniques. DSM leverages decades of soil data collection and sharing, establishing  
60 quantitative models to generate georeferenced soil maps (McBratney et al., 2003).

61  
62 Digital soil maps are typically derived from existing soil surveys, geostatistical models,  
63 machine learning, or hybrid approaches. Soil survey-based soil mapping method, which  
64 use low, high, and representative values to describe soil property distributions for each soil  
65 component (Soil Survey Staff et al., 2023). The method typically approximates each soil  
66 component as a triangular distribution (Chaney et al., 2016; Soil survey staff, 2023),  
67 potentially oversimplifying multi-modal distributions of soil properties in some cases

68 (Haghverdi et al., 2020; Nussbaum et al., 2023). Additionally, estimating soil properties  
69 from synthetic sampling within a map unit could create artificial spatial patterns, adding  
70 noises into the mapping results (Chaney et al., 2019). Developments such as Latin-  
71 hypercube sampling and landscape adaptive covariance functions have improved the  
72 representation of spatial patterns of soil properties (Minasny and McBratney, 2006). Yet,  
73 soil survey-based approaches remain valuable particularly in areas where soil profile data  
74 is limited (Nauman et al., 2024). Geostatistical models often require presumed  
75 parameterization and are constrained by stationarity assumptions, which is difficult to  
76 apply in areas with insufficient field knowledge (Oliver and Webster, 2014). To address  
77 these challenges, non-parametric models, such as Random Forest, trained with hybridized  
78 soil data that combine soil surveys with georeferenced soil profiles show potentials in  
79 improving soil mapping, particularly for large-scale maps (Chaney et al., 2019; Nauman et  
80 al., 2024).

81  
82 Map of soil properties have been observed with bias compared to field observations in  
83 certain areas due to many factors (Hengl et al., 2017; Powers et al., 2011). At the  
84 measurement level, sampling methods may favor certain landscape positions or soil  
85 conditions, causing a clustered representation (Ramcharan et al., 2018). In areas with  
86 coarse sampling density, models trained on unrepresentative data are likely to deviate  
87 from actual observations (Sharififar et al., 2019). Commonly used DSM models can show  
88 bias. For example, Random Forest classifier favors the majority class (Chen et al., 2004),  
89 and Random Forest regressors struggle to capture extreme values (Nauman et al., 2024).

90 Furthermore, certain areas may not be fully captured by the DSM model and the selected  
91 feature space, such as areas with complex glacial pattern, parent material transitions, and  
92 alluvial processes (unaddressed problem in SOLUS; SoilGrids 2.0; (Nauman et al., 2024;  
93 Poggio et al., 2021)). Model-based solutions include using ensemble models to enhance  
94 accuracy compared to a single model (Sylvain et al., 2021). Post-processing methods,  
95 such as regression kriging and bias-corrected decision trees, can also be used (Hengl et  
96 al., 2004). Yet, kriging-based methods have limitations in areas with high spatial  
97 heterogeneity and abrupt transitions, where stationary assumptions do not meet. Non-  
98 parametric models can be used for bias correction that overcome the limitation of making  
99 presumed distributions.

100

101 Quantifying uncertainties in DSM is important for its practical applications (Schmidinger  
102 and Heuvelink, 2023). DSM products represent soil properties as multi-dimensional  
103 matrices showing vertical and horizontal soil variation (Vereecken et al., 2022), with each  
104 pixel containing weighted possible values and their prediction uncertainties. These  
105 uncertainties can be represented either as continuous values through prediction intervals  
106 or as discrete classifications with associated class probabilities (Chaney et al., 2016,  
107 2019; Hengl et al., 2017; Ramcharan et al., 2018). Common quantification approaches  
108 include geostatistical techniques like kriging, where the nugget term accounts for  
109 measurement errors while kriging variance reflects spatial uncertainty patterns (Chilès and  
110 Delfiner, 2012; Takoutsing et al., 2022), and machine learning methods such as Quantile  
111 Random Forest (QRF) which generates probability distributions from decision tree outputs

112 using values of soil properties (Poggio et al., 2021; Shi et al., 2024). For discrete  
113 classifications, uncertainty derives from soil raster probabilities during soil taxa  
114 classification (Chaney et al., 2016; Odgers et al., 2015). Given the data-driven nature of  
115 DSM and frequent limitations in soil profile availability, integrating multiple qualified data  
116 sources improves the amount of soil data and reduce prediction uncertainties (Nauman et  
117 al., 2024), particularly in regions where predictions must rely more heavily on legacy soil  
118 data.

119

120 In this study, we present a hybrid DSM approach combining pruned Hierarchical Random  
121 Forest (pHRF) with iterative residual correction (IRC) method (Xu et al., 2025). The pHRF  
122 method leverages the National Cooperative Soil Survey (NCSS) soil survey data and  
123 georeferenced soil taxa information to generate prior distributions, while additional soil  
124 profiles correct biases in prior predictions. This method builds on development in previous  
125 research while addressing specific limitations. Sylvain et al. (2021) applied XGBoost  
126 (sequential decision trees) and ensemble models to correct deterministic soil property  
127 maps, demonstrating reduced bias for many soil properties (Sylvain et al., 2021). Zhang et  
128 al. (2010) introduced a bias-correction technique with Random Forest models to mitigate  
129 their tendency to regress toward mean values, though not in DSM contexts (Zhang and Lu,  
130 2012). Our approach extends these concepts by probabilistically updating posterior  
131 distributions at each location through an iterative correction process that continues until  
132 convergence across vertical intervals. Vertical correlations are maintained through layer-  
133 by-layer residual correction, which preserves inter-layer correlations while dynamically

134 optimizing the feature space at each correction step. Unlike methods requiring  
135 distributional assumptions, our non-parametric framework adapts to diverse landscapes  
136 and data scenarios. The models implement residual correction by minimizing the  
137 differences between priors and new observations to adjust posterior distributions, with the  
138 entire process continuing until property variations stabilize between different iterations.  
139 This method aims to improve the accuracy and reliability of soil property maps, supporting  
140 decision-making in relevant applications.

141

## 142 **2 Methods**

143 This study introduces a hybrid framework for digital soil mapping (DSM) that updates  
144 existing probabilistic soil property maps using newly collected soil observations. The  
145 framework combines prior soil property estimates with an iterative residual correction  
146 (IRC) method. The IRC method integrates additional georeferenced soil profiles (soil  
147 observations not used to train prior soil maps) and employs non-parametric models to  
148 adjust the distribution of prior estimates, thereby correcting biases in the prior soil maps.

149

150 The following sections first describe the general residual correction framework (Section  
151 2.1). To illustrate the method concretely, we then provide a worked example using one  
152 randomly selected soil column to demonstrate how the feature space is constructed and  
153 updated across two consecutive iterations (Section 2.1.1). Building on this example, we  
154 detail the key components of the IRC method: the iterative update of feature space  
155 (Section 2.1.2), the convergence criteria for residual correction (Section 2.1.3), and the

156 process for updating posterior soil properties with physical constraints (Section 2.1.4).  
157 Finally, we present the California case study (Section 2.2), describing the soil datasets  
158 used (Section 2.2.1) and the implementation details for applying the IRC method over  
159 California (Section 2.2.2).

160

### 161 **2.1 Iterative Residual Correction Framework for DSM**

162 Residual correction is implemented to address underestimated soil property variation in  
163 prior maps (tendency to underestimate high values and overestimate low values,  
164 smoothing out soil variation across landscape). The overall workflow of the IRC method  
165 consists of three components: (1) prior map generation (Figure 1a), (2) residual preparation  
166 (Figure 1b), and (3) iterative correction (Figure 1c).

167

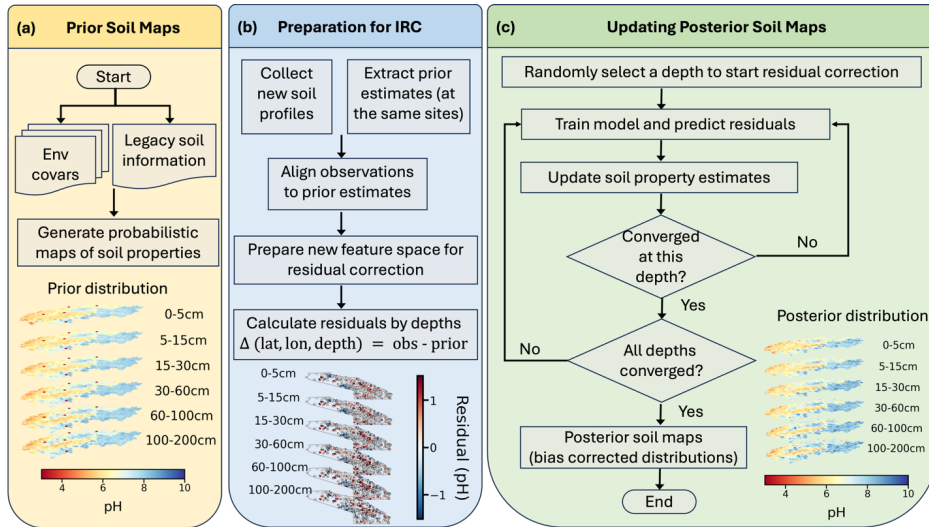
168 First, probabilistic prior soil property maps are generated or retrieve probabilistic soil  
169 property maps from an existing DSM product as the prior soil maps (Figure 1a). These  
170 maps represent the initial estimates of soil properties and their associated uncertainties.  
171 Second, a residual preparation step is carried out to enable correction using new soil  
172 profile observations (Figure 1b). The preparation involves four key steps: (1) adding  
173 additional soil profiles from new field measurements or databases; (2) spatially aligning  
174 these profiles with the corresponding pixels in the prior soil maps using geographic  
175 coordinates; (3) vertically aligning observations with prior predictions at matching depth  
176 intervals; and (4) calculating residuals depth by depth as the difference between observed  
177 values and prior predictions. During this stage, the feature space for residual modeling is

178 also prepared, consisting of static environmental covariates (which remain fixed  
179 throughout iterations) and dynamic soil covariates (which are updated iteratively). Detailed  
180 construction of the feature space is described in Section 2.1.1.

181

182 Finally, iterative residual correction is performed to update soil property estimates across  
183 depths (Figure 1c). During each iteration, the model predicts residuals for one depth layer  
184 at a time, with the layer selected randomly. A Random Forest regressor is trained to learn  
185 the relationship between residuals and the feature space at sampled locations, then  
186 interpolates residual corrections across the study area. Predicted residuals are added to  
187 the prior (or previous iteration's) estimates to generate updated soil property values. After  
188 each update, convergence is evaluated for the modeling depth by comparing the median  
189 difference between the current residuals and those from the previous iteration. Once this  
190 change falls below a predefined threshold, that depth is considered converged and  
191 excluded from subsequent updates. The algorithm then focuses on the remaining  
192 “unconverged” depths, until convergence is achieved across all layers. After convergence  
193 is verified for all depths, the final corrected residuals are added to the prior estimates to  
194 update the posterior distributions of soil properties.

195



196  
 197 Figure 1: Workflow for updating posterior soil property maps. The process begins with  
 198 panel (a), the preparation of environmental covariates (env covars) to generate  
 199 probabilistic maps of soil properties (prior soil maps). As illustrated in panel (b), the  
 200 preparation for residual correction involves adding additional soil profiles, spatially and  
 201 vertically aligning prior soil map values with new profile observations, calculating residuals  
 202 depth by depth, and preparing environmental covariates and soil covariates (new feature  
 203 space) for residual correction. Finally, as shown in panel (c), the iterative residual  
 204 correction step applies bias corrections across different depths, focusing on layers where  
 205 residuals have not yet stabilized. During each iteration, the model predicts residuals for  
 206 one depth at a time, randomly selecting a layer. Once residuals for a given depth converge,  
 207 that layer is excluded from further updates, allowing the model to concentrate on  
 208 remaining depths until all achieve stability. After verifying convergence across all depths,

209 the algorithm updates the posterior distribution of soil properties and produces the final  
210 soil maps (posterior soil property maps).

211  
212 In this IRC framework, "prior probabilistic soil property maps" refer to spatially continuous  
213 soil property maps that provide an initial (prior) estimate of soil properties with associated  
214 uncertainty across the study area. These prior maps provide, for each pixel and depth  
215 interval, a distribution of possible soil property values with associated probabilities or  
216 weights. The IRC method does not require prior and new soil observations to be co-located  
217 at the same pixels. Instead, the method requires that a prior estimate exists at locations  
218 where new soil observations are available. By learning the relationship between residuals  
219 (differences between new observations and prior estimates) and environmental and soil  
220 covariates at sampled locations, the trained model can interpolate residual corrections  
221 across the study area.

222

### 223 **2.1.1 Worked Example**

224 The iterative residual correction method is further illustrated in Figure 2 using an example  
225 with a randomly selected soil column. Figure 2a shows the location of the selected soil  
226 column, where additional soil profile observations are available. The right panel displays  
227 the top-3 probable pH values (from prior soil maps) at each depth intervals (0–5 cm, 5–15  
228 cm, 15–30 cm, 30–60 cm, 60–100 cm, 100–200 cm), while the left panel shows the three  
229 weights (probabilities) associated with these pH values. In this simplified example, we use  
230 3 bins to represent the soil property distribution; however, in actual implementation, more

231 bins are maintained (typically top-12 probable values) to better capture soil variability. For  
232 this demonstration, Depth 2 ( $D_2$ ; 5–15 cm) is randomly selected as the modeling layer to  
233 initiate the iterative correction process. Only one layer is modeled and updated for a given  
234 iteration. Note that in real model execution, model generally processes over 3,000 soil  
235 columns simultaneously in California, though only one column is shown here for clarity.

236

237 In Figure 2b, the table details features used to train the Random Forest regressor for  
238 residual prediction. The feature space consists of environmental covariates that remain  
239 fixed across iterations and soil covariates that are updated iteratively:

240 (1) Environmental covariates (21 dimensions): These capture spatial variations in  
241 soil-forming factors and remain unchanged throughout all iterations. The covariates  
242 include remote sensing data (Sentinel-1, Sentinel-2, GOES land surface  
243 temperature) and terrain attributes, identical to those used in the prior mapping  
244 method (Xu et al., 2025).

245 (2) Depth information (1 dimension): The centroid (median value) of the soil depth  
246 interval for the modeling layer (e.g., 10 cm for the 5–15 cm layer), describing the  
247 vertical position in the soil profile.

248 (3) Representative soil property values (1 dimension): The expected value (weighted  
249 mean) of the soil property at each pixel in the modeling layer, representing the  
250 current best estimate. This is computed as the weighted sum of top-probable  
251 values.

252 (4) Top-probable soil property values (1 dimension): The current predictions at each  
253 pixel (residuals plus previous prediction of soil property values), reflecting both  
254 intra-pixel and inter-pixel soil heterogeneity.

255 (5) Inter-layer differences (5 dimensions): Differences in top-probable predicted soil  
256 property values between the modeling layer and the other five depth layers. For  
257 instance, if modeling Depth 2, the inter-layer differences would be  $(D_2-D_1)$ ,  $(D_2-D_3)$ ,  
258  $(D_2-D_4)$ ,  $(D_2-D_5)$ , and  $(D_2-D_6)$ . These features capture vertical correlations in the soil  
259 profile and aid in estimating spatial patterns.

260 (6) Weights (1 dimension): Probabilities associated with each top-probable soil  
261 property value. These weights remain fixed throughout iterations.

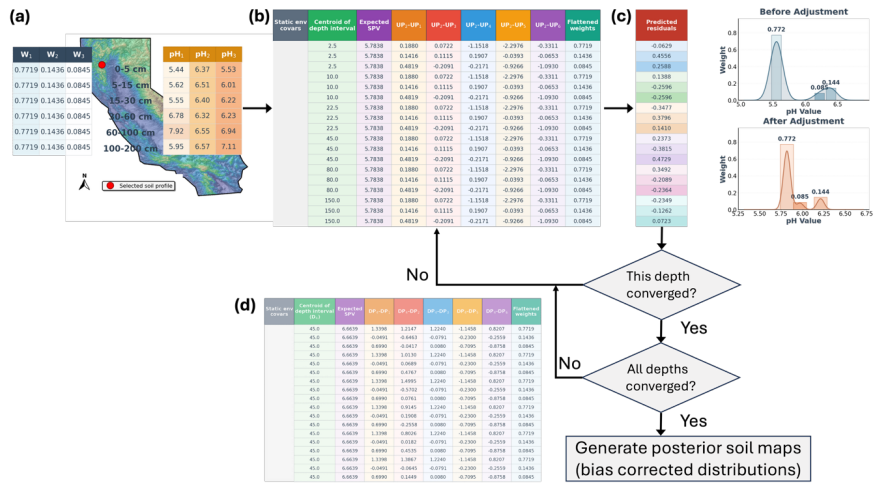
262

263 In summary, environmental covariates and weights remain static, while depth information,  
264 representative values, top-probable values, and inter-layer differences are updated across  
265 iterations based on the most recent soil property estimates.

266

267 A Random Forest regressor is then trained using the feature space to predict residuals for  
268 the modeling layer ( $D_2$  in this example). The right panel in Figure 2c compares the  
269 distribution of pH values before and after residual adjustment in the current iteration. After  
270 applying the residual correction, convergence is checked for  $D_2$  by comparing the median  
271 difference between the current and previous residuals. If  $D_2$  has converged (difference  
272 below threshold), the algorithm proceeds to check whether all depth layers have  
273 converged. If all layers have converged, the iterative process terminates, and the final

274 posterior soil property maps are generated by adding the last predicted residuals to the  
275 prior values.  
276  
277 If either convergence check returns "No" (i.e.,  $D_2$  has not converged or other layers remain  
278 unconverged), the algorithm continues iterating. Here, the soil property values for  $D_2$  are  
279 updated by adding the predicted residuals to the previous pH values. These updated  
280 values are then used to reconstruct the feature space following the same structure  
281 described above, updating the representative values, top-probable values, and inter-layer  
282 differences. By updating soil covariates layer by layer and iteratively refining the feature  
283 space, the next prediction retains prior knowledge while integrating new information about  
284 soil heterogeneity and vertical relationships for soil profiles (Wu et al., 2025). A new  
285 iteration begins by randomly selecting another unconverged layer, and the process repeats  
286 until convergence is achieved across all depth layers.  
287



288  
 289 Figure 2: Schematic illustration of the iterative residual correction (IRC) method using a  
 290 worked example at a randomly selected soil column. (a) Prior distributions and  
 291 observation location: The map shows the location of the selected soil column within the  
 292 study area. The right panel displays the top-3 probable pH values at each of the six depth  
 293 intervals (0–5 cm, 5–15 cm, 15–30 cm, 30–60 cm, 60–100 cm, 100–200 cm), while the left  
 294 panel shows the three weights ( $w_1$ ,  $w_2$ ,  $w_3$ ) associated with these pH values. Depth 2 ( $D_2$ ; 5–  
 295 15 cm) is randomly selected for this iteration. (b) Feature space components: The table  
 296 details the structure of the feature space used to train the Random Forest regressor for  
 297 residual prediction. The feature space comprises both static and dynamic components.  
 298 Static components include environmental covariates (satellite imagery, terrain attributes)  
 299 that remain unchanged throughout iterations, and weights ( $w_1$ ,  $w_2$ ,  $w_3$ ) associated with top-  
 300 probable values. Dynamic soil covariates that are updated in each iteration include: the  
 301 centroid of the depth interval (e.g., 10 cm for  $D_2$ ), the expected (representative) soil

302 property value computed as the weighted mean, the top-probable soil property values  
303 reflecting intra-pixel heterogeneity, and inter-layer differences capturing vertical  
304 correlations (e.g.,  $D_2-D_1$ ,  $D_2-D_3$ ). (c) Residual correction and convergence workflow: A  
305 Random Forest model trained on the feature space predicts residuals for the modeling  
306 layer  $D_2$ . The right panel compares the pH distribution before and after residual  
307 adjustment. The flowchart below describes the convergence logic: after predicting and  
308 applying residuals to  $D_2$ , the algorithm evaluates whether  $D_2$  has converged. If  $D_2$  has  
309 converged, the algorithm checks whether all depth layers have achieved convergence. If  
310 both checks pass, the final posterior soil property maps are generated by adding the last  
311 converged residuals to the prior values. (d) If either check fails, the algorithm updates the  
312 soil property values for  $D_2$  by adding predicted residuals, reconstructs the feature space  
313 with the updated values, randomly selects another unconverged layer, and repeats the  
314 process. This iterative cycle continues until convergence is achieved across all six depth  
315 layers.

316

### 317 **2.1.2 Convergence of Residual Correction**

318 The residual correction process continues until the median difference between updated  
319 residuals and previous residuals falls below a predefined threshold. Convergence is  
320 achieved when the residuals stabilize across multiple iterations, indicating that further  
321 adjustments do not largely change the predictions. This stability ensures that the final  
322 posterior soil properties are reliable and consistent. The stopping criterion is a  
323 customizable parameter. In this work, it was set to the 5th percentile of the distribution of

324 value changes. To avoid over-correcting bias, only the last converged residuals are added  
325 to the prior prediction to generate the final posterior results.

326

### 327 **2.1.3 Update with Constraints**

328 During residual correction, a common issue arises where the addition of residuals to prior  
329 soil property values results in values that exceed physical bounds (such as sand content >

330 100%; fine-earth fraction in mass). To address this, a residual update process with

331 constraints is implemented.

332

333 As illustrated in Figure 2c to 2d, after the Random Forest regressor predicts residuals for  
334 the layer ( $D_2$ ), these residuals are added to the previous soil property values to generate  
335 updated predictions. Immediately after this addition step, the updated values are  
336 examined to check whether they fall within predefined physical bounds (e.g., 0% to 100%  
337 for particle size fractions, positive values for bulk density). This constraint check occurs  
338 before the convergence evaluation and before the updated values are used to reconstruct  
339 the feature space for the next iteration.

340

341 If any updated value exceeds the physical bounds, it is adjusted to the nearest valid bound  
342 (minimum or maximum). For example, if adding a residual of +15% to a prior sand content

343 of 90% yields 105%, this value is capped at 100% (mass fraction). The "excess" residual

344 (+5% in this case) is then redistributed proportionally (based on their weights) among the

345 other top-probable values at the same pixel, ensuring that the total correction remains

Deleted: %).

Deleted: %.

348 consistent with the model's prediction while maintaining physical plausibility. For particle  
349 size fractions (sand, silt, clay), an additional compositional constraint ensures that the  
350 three fractions sum to 100% at each pixel after residual correction.

351

## 352 **2.2 California Case Study: Soil Data and Model Implementation**

### 353 **2.2.1 Soil Data**

354 To demonstrate the IRC method, we apply it to soil property mapping in California. We use  
355 georeferenced soil profiles with laboratory measurements of soil properties. We compiled  
356 soil profile data from three primary sources: the World Soil Information Service (WoSIS),  
357 the National Soil Characterization Database (SCD), and field measurements conducted in  
358 California (Batjes et al., 2024; National Cooperative Soil Survey, 2018; Scudiero et al.,  
359 2024).

360

361 To ensure consistency across different data sources, we applied several quality control  
362 steps. First, we checked the physical plausibility of all soil property values by defining a  
363 valid range with specific minimum and maximum thresholds for each property. Any data  
364 point falling outside these ranges was considered an error and removed. For soil texture,

365 we required the sum of sand, silt, and clay fractions to equal 100% (mass fraction). If a  
366 profile did not meet this compositional constraint, it was excluded. After quality check, the  
367 datasets are compatible because the WoSIS records for California are largely derived from  
368 the NCSS database, and both the SCD and WoSIS datasets follow standardized laboratory  
369 protocols, such as those from the Kellogg Soil Survey Laboratory (Soil, 1996; Soil Survey

Deleted: %.

371 Staff, 2014). For our own field measurements, we used the Integral Suspension Pressure  
372 (ISP+) method to maintain precision for particle size analysis (Corwin and Scudiero, 2020;  
373 Scudiero et al., 2024).

374

375 During preprocessing, we harmonized all soil data, which was originally reported at  
376 different soil horizons, into six standard depth intervals: 0–5 cm, 5–15 cm, 15–30 cm, 30–  
377 60 cm, 60–100 cm, and 100–200 cm (Arrouays et al., 2014). The harmonization was  
378 performed using equal-area spline functions to interpolate soil property values from the  
379 original horizon depths to these standard intervals (Hartemink et al., 2010, p.201). The  
380 spline function fits a smooth curve through observed values at their measured depths,  
381 then calculates the area under this curve within each standardized depth interval and  
382 divides by the interval width to obtain the value. Location of soil profiles and their  
383 distribution of soil property values are presented in Figure 3. Six soil properties are studied:

384 sand content (% mass), silt content (% mass), clay content (% mass), pH, soil organic  
385 matter (log-scaled % mass), and oven-dry bulk density ( $\text{g cm}^{-3}$ ). These samples were not  
386 co-located with the training samples used to generate the prior maps (samples at the  
387 same locations were already removed). The number of observations varies by soil property:  
388 pH has the most samples, followed by oven-dry bulk density and soil organic matter. The  
389 sample sizes across properties can also be inferred from the frequency histograms shown  
390 in the lower-left corner of each panel in Figure 3. Across all depths combined, each soil  
391 property has more than 11000 observations in California. The number of observations

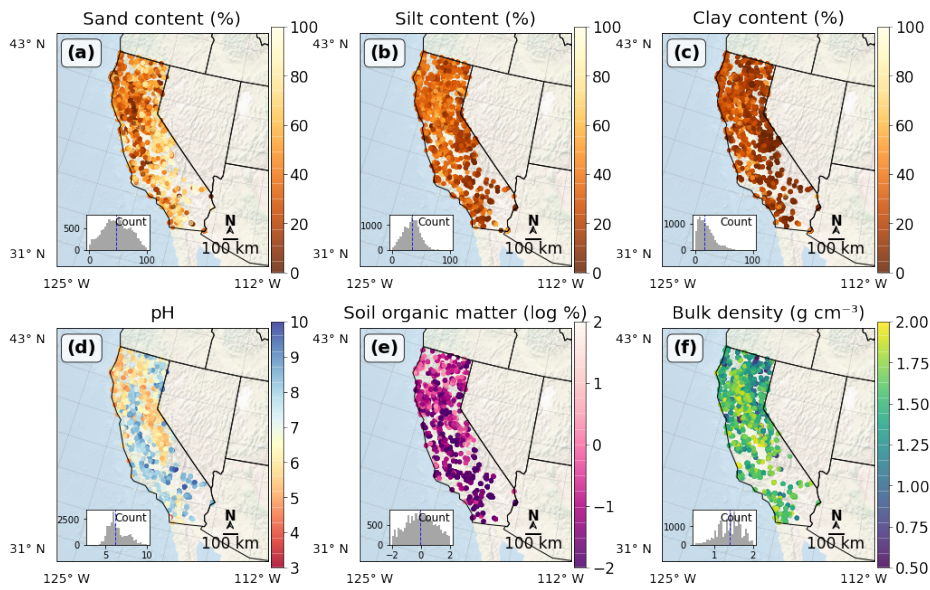
Deleted: ,

Deleted: ,

Deleted: ,

Deleted: .

396 generally decreases with depth, with depths below 1 m having notably fewer samples  
 397 compared to shallower layers.  
 398



399  
 400 Figure 3: Spatial distribution and statistical characteristics of soil properties observations  
 401 across California. The figure presents six soil parameters mapped using an Albers Equal  
 402 Area projection: (a) sand content (% mass), (b) silt content (% mass), (c) clay content (%  
 403 mass), (d) pH, (e) soil organic matter (log-scaled % mass), and (f) bulk density ( $\text{g cm}^{-3}$ ).  
 404 Each subplot displays sample locations as colored points, with field-collected samples  
 405 shown as triangles to distinguish them from WoSIS (circles) and SCD (squares) samples.  
 406 Distribution histograms in the lower left corner of each subplot show the frequency  
 407 distribution of values, with blue dashed lines indicating median values. Distance scale bar  
 408 and compass rose are provided in the right corner. Note that the total number of soil

Deleted: (  
 Deleted: %),  
 Deleted: (  
 Deleted: %),  
 Deleted: (  
 Deleted: %),  
 Deleted: %),  
 Deleted:  $\text{g/cm}^3$ ).

417 measurements varies by property and generally decreases with depth beyond the surface  
418 layer, with the surface layers and depths below 1 m generally having fewer observations.

419

#### 420 **2.2.1.1 World Soil Information Service (WoSIS)**

421 The World Soil Information Service (WoSIS), managed by the International Soil Reference  
422 and Information Centre (ISRIC), aggregates global soil data from diverse sources, including  
423 national soil institutes, research organizations, and collaborative initiatives like the Global  
424 Soil Partnership (GSP) and the International Network of Soil Information Institutions (INSII).

425 The database provides soil properties for different soil horizons, georeferenced in decimal  
426 degrees, and undergoes quality controls (Batjes et al., 2024). In California, WoSIS typically  
427 offers 2,000 to over 5,000 soil observations for the modeling soil property. Samples below

428 1 m depth are fewer than those from shallower layers.

429

#### 430 **2.2.1.2 Soil Characterization Database (SCD)**

431 The Soil Characterization Database (SCD) is a subset of the National Cooperative Soil  
432 Survey (NCSS) database (National Cooperative Soil Survey, 2018). It records soil properties  
433 for each soil horizon within a soil profile (pedon), including soil texture, bulk density, and  
434 water retention. In California, SCD provides between 500 and over 1,000 soil samples per  
435 layer for the studied soil property. Each soil profile is georeferenced and includes  
436 metadata such as site location, land use, and sampling methods.

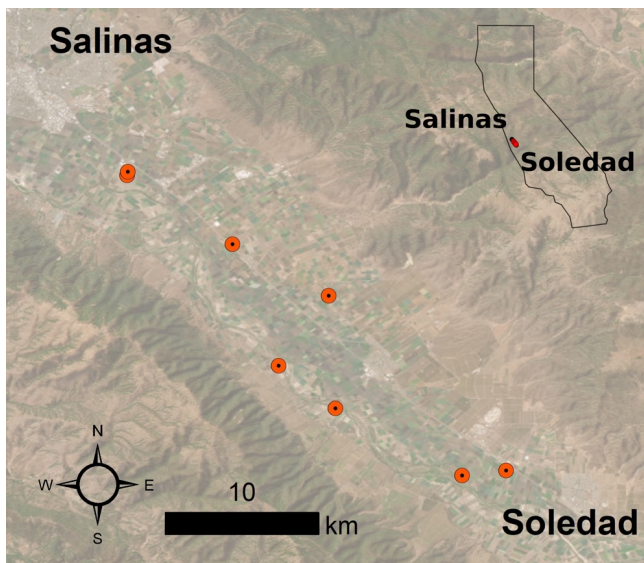
437

Deleted: -

439 **2.2.1.3 Ground Truth Soil Sampling and Measurements**

440 Additional soil sampling was conducted to complement georeferenced soil profiles in  
441 California for model training and evaluation. These data are reported in (Scudiero et al.,  
442 2024) and are briefly discussed here. Multiple fields located between Salinas and Soledad  
443 in California's Salinas Valley were selected to collect soil particle size fraction data (Figure  
444 4). These fields, presented as red dots in Figure 4, were chosen because they were  
445 accessible, unfarmed during the sampling period, and spread across different parts of the  
446 valley.

447



448  
449 Figure 4: Map of sampling fields in the Salinas Valley in California. Each red dot represents  
450 a sampling field between Salinas and Soledad. An inset map (top right) shows the location  
451 of the sampling area within California. Scale bar and direction indicator are provided in the

452 left corner. *Basemap: Esri World Imagery. Source: Esri, Maxar, Earthstar Geographics, and*  
453 *the GIS User Community.*

454

455 Soil apparent electrical conductivity (ECa) was measured across fields using an  
456 electromagnetic induction (EMI) sensor connected to a GPS receiver. Following the ECa-  
457 directed soil sampling protocols of Corwin and Scudiero (Corwin and Scudiero, 2020), the  
458 most representative soil samples were identified with ESAP software package and the  
459 Response Surface Sampling Design algorithm (Lesch et al., 2000; Lesch, 2005). 0-0.8 and  
460 0-1.6 m soil profiles were further analyzed and followed with the expectation that ECa was  
461 a regional proxy for the field-scale variability of particle size fraction.

462

463 To measure particle size fraction, soil samples were then collected from multiple depths  
464 (0–0.1, 0.1–0.4, and 0.4–1.2 m) across fields. After collection, the samples were air-dried,  
465 ground, and sieved to remove particles larger than 2 mm; and then measured using the  
466 Integral Suspension Pressure method (The improved integral suspension pressure method  
467 (ISP+) for precise particle size analysis of soil and sedimentary materials; Wolfgang Durner,  
468 Sascha C. Iden) using PARIO™ system (METER Group AG, Munich, Germany).

469

### 470 **2.2.2 Model Implementation for the California Case Study**

471 For the California case study, prior soil property maps were generated using the pruned  
472 hierarchical Random Forest (pHRF) method (Xu et al., 2025). The pHRF-derived soil maps  
473 were developed with soil pedons from the National Soil Information System (NASIS) and

474 part of SCD (the remaining data not used in IRC method). After gaining prior estimate of soil  
475 properties, the IRC method was then applied using the additional soil observations from  
476 WoSIS, SCD, and field measurements, which were not used in generating the prior maps.  
477 The convergence threshold for each soil property was set to the 5th percentile of the  
478 distribution of value changes between iterations.

479  
480 Model training and evaluation were performed using out-of-bag (OOB) sampling, with OOB  
481 samples (samples withheld from the training process and not used to fit the models) that  
482 shared the same geolocation as training samples removed to prevent data leakage and  
483 reduce spatial autocorrelation effects. In each iteration, a new Random Forest model is  
484 trained to update residuals for one specific depth interval, and the same set of OOB  
485 samples remains excluded throughout to ensure independent validation.

486

### 487 **3 Results**

488 The iterative residual correction (IRC) method is applied to adjust pHRF-derived prior soil  
489 properties, including particle size fractions (mass percentage of sand content, silt content,  
490 and clay content), pH, oven-dry bulk density (BD; g cm<sup>-3</sup>), and soil organic matter (SOM;  
491 log-scaled mass percentage) over California. This correction addresses biases in the prior  
492 soil property maps and updates the posterior distributions of these properties. These soil  
493 properties are important for land management and serve as essential inputs for  
494 pedotransfer functions. The residual correction is performed across California, covering  
495 six depth intervals: 0-5 cm, 5-15 cm, 15-30 cm, 30-60 cm, 60-100 cm, and 100-200 cm.

Deleted: ,

Deleted: ),

498

### 499 3.1 Performance Evaluation of Posterior Soil Properties

500 Table 1 presents the performance metrics for the posterior predictions of six key soil  
501 properties: mass percentage of sand content, silt content, and clay content (% mass), pH,  
502 oven-dry bulk density (BD;  $g\ cm^{-3}$ ), and soil organic matter (SOM; mass percentage). The  
503 metrics include the root mean square error (RMSE), coefficient of determination ( $R^2$ ), and  
504 correlation coefficient ( $\rho$ ). For example, sand prediction (% mass) shows an RMSE of  
505 9.322, an  $R^2$  of 0.841, and a correlation coefficient of 0.918. pH prediction shows an RMSE  
506 of 0.270, an  $R^2$  of 0.945, and a correlation coefficient of 0.972. These metrics are computed  
507 using out-of-bag (OOB) samples from random forest regressors. OOB samples are data  
508 points not included in the bootstrap samples used to train each tree in the random forest.  
509 Additionally, these metrics are evaluated by comparing the expected values of posterior  
510 predictions with co-located soil properties values; not computed on residuals.

511

512 Table 1 also shows variations in performance across different soil properties. SOM and  
513 bulk density show slightly worse metrics compared to particle size fractions and pH. For  
514 instance, SOM predictions (mass percentage) have an RMSE of 1.961, an  $R^2$  of 0.608, and a  
515 correlation coefficient of 0.801, and bulk density predictions ( $g\ cm^{-3}$ ) have an RMSE of  
516 0.164, an  $R^2$  of 0.704, and a correlation coefficient of 0.843. Two main reasons can result in  
517 their lower performance. First, these properties are more dynamic in nature compared to  
518 particle size fractions and pH. SOM and bulk density can change over time due to factors  
519 such as land use practices. The prior predictions are trained using soil survey data that are

Deleted: ,

Deleted: ,

Deleted: ),

523 older, while the posterior soil profiles used for evaluation may come from a different  
 524 period. Second, SOM and bulk density are more challenging to model accurately. SOM is  
 525 influenced by complex biological and soil-forming processes, such as decomposition  
 526 rates and organic matter inputs. Similarly, bulk density is affected by soil compaction,  
 527 organic matter content, and soil structure. All of them can vary spatially and temporally.  
 528 Depth-wise analysis of model performance is provided in the Supplementary Information  
 529 (Table S1 and S2).

530

531 **Table 1: Performance metrics (RMSE,  $R^2$ , and correlation coefficient  $\rho$ ) for posterior**  
 532 **predictions of soil properties, including sand, silt, clay, pH, oven-dry bulk density**  
 533 **(BD), and soil organic matter (SOM). The table summarizes the range (minimum and**  
 534 **maximum values) and accuracy metrics for each property averaged across all depth**  
 535 **intervals.**

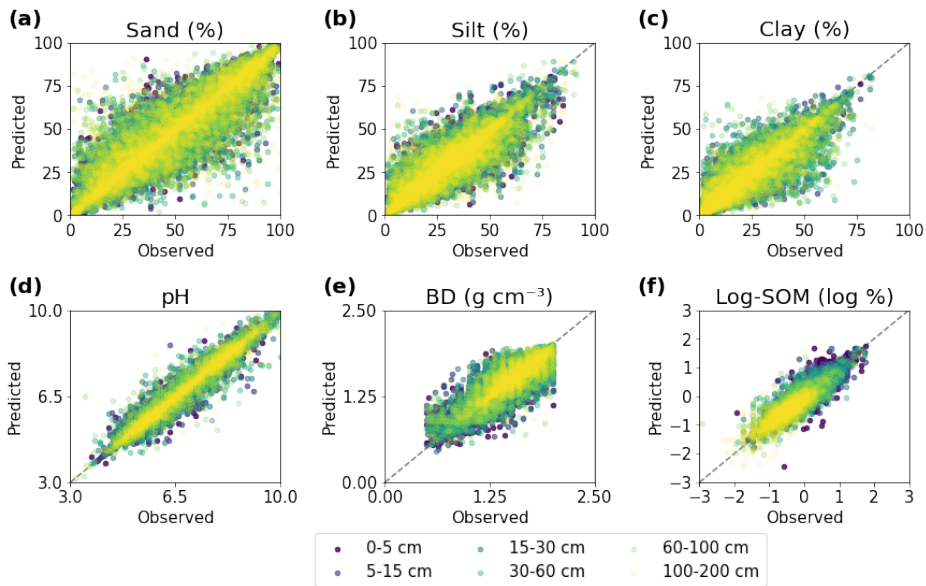
Property	Unit	Min	Max	RMSE	$R^2$	$\rho$
Sand	% mass	0.0	100.0	9.322	0.841	0.918
Silt	% mass	0.0	100.0	6.556	0.788	0.889
Clay	% mass	0.0	100.0	5.891	0.841	0.918
pH	$\log_{10}([H^+])$	3.0	10.0	0.270	0.945	0.972
BD (oven-dry)	<del>g</del> $\text{cm}^{-3}$	0.5	2.0	0.164	0.704	0.843
SOM	% mass	0.0	100.0	1.961	0.608	0.801

Formatted Table

Deleted: g/cm<sup>3</sup>

537  
538 The posterior predictions of soil properties all align with the co-located observations and  
539 can capture the general trend of observations (Figure 5). Predictions of pH show the most  
540 concentrated clustering to the dashed line, indicating good agreement with observations  
541 across all depths. SOM and bulk density show relatively weaker performance compared to  
542 other predicted soil properties. And this pattern of reduced accuracy persists throughout  
543 all depths.

544  
545 As Figure 5 shows, the performance of the model tends to decline with increasing soil  
546 depth, except for SOM. This decline is primarily due to several reasons. First, the  
547 availability of soil data is often greater for shallower layers compared to deeper layers  
548 (such as > 1 m), which limits the model's ability to learn patterns in deep layers. Second,  
549 remote sensing-derived soil covariates can only observe surface properties. Predictions  
550 for deeper layers rely on soil horizon information, soil profiles, geology, and parent  
551 material-related features. The certainty and quantity of them are less than easily  
552 measurable surface covariates. However, SOM shows better performance in deeper layers  
553 compared to surface layers. This is likely because surface SOM is highly variable due to  
554 factors like residue, land use, and management practices, while deeper SOM tends to be  
555 more stable.



556  
 557 **Figure 5: Evaluating posterior predictions with observations for six soil properties: (a)**  
 558 **sand (% mass), (b) silt (% mass), (c) clay (% mass), (d) pH, (e) bulk density (BD;  $g\ cm^{-3}$ ),**  
 559 **and (f) log-scaled soil organic matter (SOM; log % mass).** The left side shows scatter  
 560 **plots of posterior predictions versus observations across six depth intervals, with**  
 561 **each depth represented by a distinct color. The dashed black line represents perfect**  
 562 **prediction.**

563

### 564 3.2 Comparison of Prior and Posterior Soil Predictions

565 Prior and posterior predictions of soil properties are compared against co-located  
 566 observations to assess the added value of residual correction. The radar plots in Figure 6  
 567 illustrate the improvements achieved through the residual correction method using three  
 568 normalized unitless metrics: 1-normalized absolute bias ( $1-|Bias|$ ), coefficient of

Deleted: ,  
 Deleted: ,  
 Deleted: ,  
 Deleted: ,

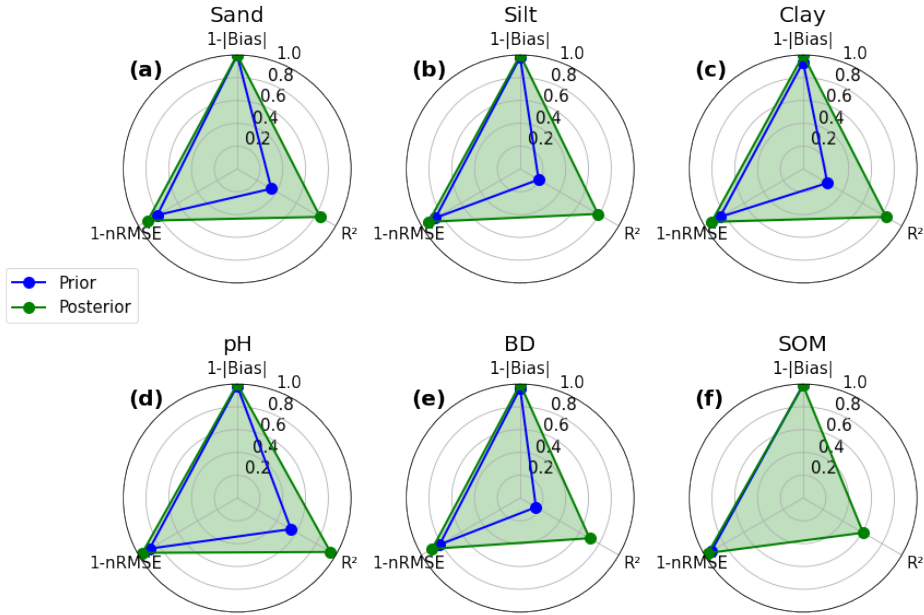
573 determination ( $R^2$ ), and 1-normalized RMSE by ranges of soil variability (1-nRMSE). These  
574 metrics are computed with values of soil properties, instead of on their residuals. Values in  
575 Figure 6 closer to the outer edge of each plot indicate better model performance. Overall,  
576 all soil properties maintain reasonable normalized bias and nRMSE (with nRMSE values  
577 consistently less than 0.2 for both prior and posterior predictions). However, the prior  
578 predictions tend to underestimate the variability of soil properties. As a result, the  
579 normalized metrics for prior and posterior predictions are similar, while the  $R^2$  values show  
580 some differences.

Deleted: 02

581  
582 For all soil properties, posterior predictions consistently outperform prior predictions  
583 across all metrics. For particle size fractions,  $R^2$  values show the largest improvements:  
584 sand increases from 0.35 to 0.84, silt from 0.19 to 0.79, and clay from 0.25 to 0.84. The  
585 nRMSE metric also shows improvements. Sand decreases from 0.19 to 0.09, silt from 0.14  
586 to 0.07, and clay from 0.16 to 0.07, showing reductions in prediction errors using the  
587 residual correction.

588  
589 Aggregating data from all depths, Figure 6 shows the degree of improvement across  
590 different soil properties. Prior pH predictions already demonstrate reasonable accuracy,  
591 with an  $R^2$  of 0.54 and nRMSE of 0.11. After the residual correction, these metrics improve  
592 to 0.94 for  $R^2$  and 0.04 for nRMSE. Bulk density and SOM show the biggest gains. For bulk  
593 density, the  $R^2$  increasing from 0.16 to 0.70 and nRMSE reducing from 0.18 to 0.11. Prior

595 SOM are underfitted with a low  $R^2$  value. With the residual correction, the posterior SOM  
 596 show a positive  $R^2$  of 0.61. The nRMSE for SOM also improves from 0.07 to 0.04.



597  
 598 **Figure 6: Radar plots comparing the performance metrics of prior and posterior**  
 599 **predictions for six soil properties: (a) sand (% mass), (b) silt (% mass), (c) clay (%**  
 600 **mass), (d) pH, (e) oven-dry bulk density (BD;  $g\ cm^{-3}$ ), and (f) soil organic matter (SOM;**  
 601 **log % mass). Each plot presents three metrics: 1-normalized absolute bias (1-|Bias|),**  
 602 **coefficient of determination ( $R^2$ ), and 1-normalized RMSE by ranges of soil variability**  
 603 **(1-nRMSE). Prior predictions are shown in blue, and posterior predictions in green. All**  
 604 **metrics are scaled from 0 to 1, where values closer to the outer edge of the plot**  
 605 **indicate better model performance. The green shaded area highlights the**  
 606 **improvement achieved by the posterior predictions over prior estimates.**

Deleted: ,  
 Deleted: ,  
 Deleted: ,  
 Deleted: ),

611  
612 Horizontal spatial patterns of the six soil properties are presented in Figure 7. In the  
613 Central Valley California, soils are mostly medium textured with about 30% silt and lower  
614 sand content compared to surrounding areas. In the Mojave and Colorado Deserts, high  
615 sand contents (> 60% mass) with low clay contents are observed. SOM contents are also  
616 low in these areas. The histograms show how residual correction adjusts the distribution of  
617 soil properties.

Deleted: %)

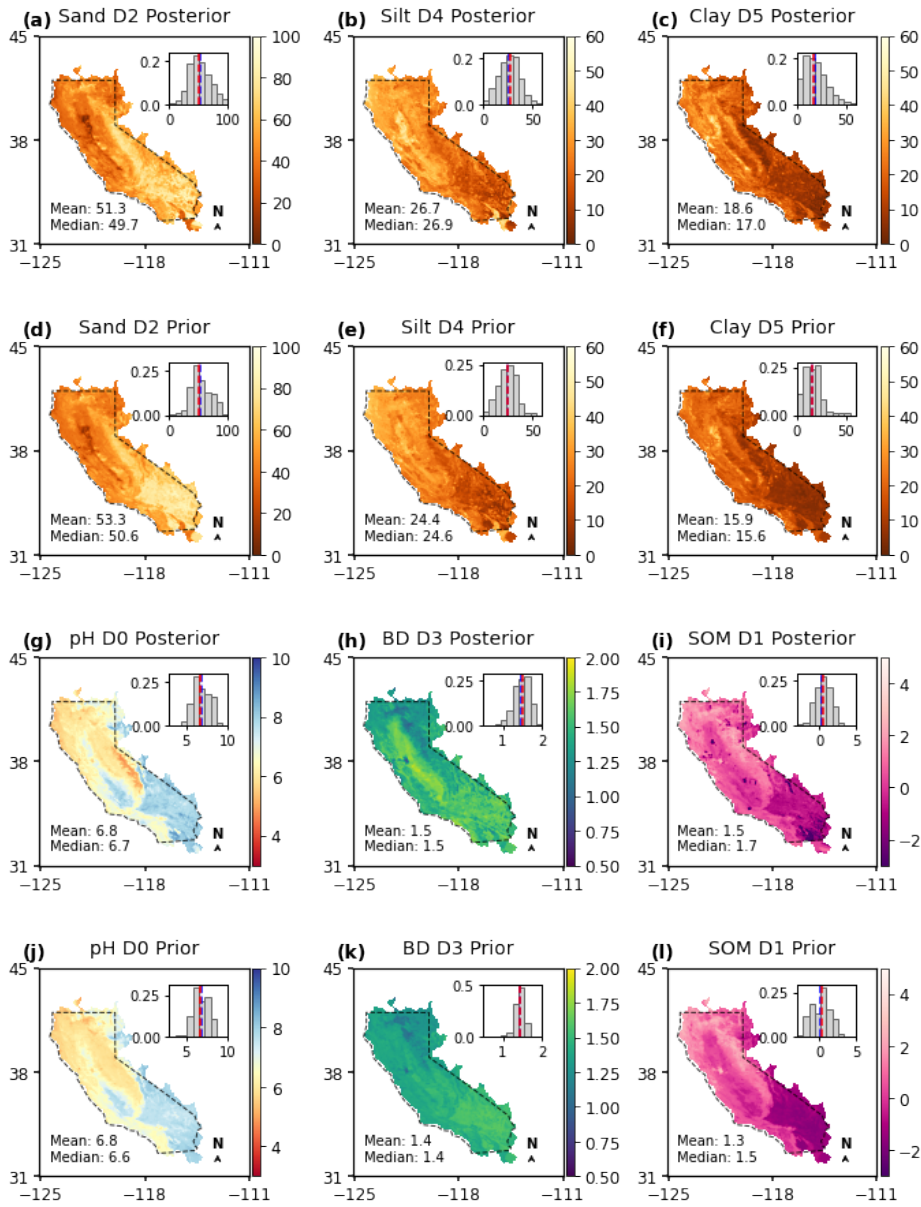
618  
619 For SOM and bulk density, the prior predictions often underestimate the observed  
620 variation. Figure 7 shows that the residual correction processes add noticeable spatial  
621 variations between prior and posterior soil maps. Prior bulk density values are often  
622 clustered around  $1.5 \text{ g cm}^{-3}$ , whereas the posterior histogram presents a broader range,  
623 spanning from  $1.25 \text{ g cm}^{-3}$  to  $1.6 \text{ g cm}^{-3}$ , capturing more heterogeneity of bulk density.

Deleted:  $\text{g/cm}^3$ ,

Deleted:  $\text{g/cm}^3$

Deleted:  $\text{g/cm}^3$ ,

624 Similarly, the residual correction adds soil heterogeneity to SOM. The posterior SOM can  
625 delineate water bodies, where SOM content is abruptly lower than the surrounding areas.  
626 Additionally, the posterior SOM maps present hill features in the desert areas.



631

632 **Figure 7: Spatial distribution of six soil properties: sand (% mass), silt (% mass), clay**

Deleted: (  
Deleted: ,  
Deleted: ,

636 content (~~% mass~~), pH, bulk density (~~g cm<sup>-3</sup>~~), and soil organic matter (~~log % mass~~)  
637 across California. Maps of prior and posterior soil properties are compared. The  
638 corresponding frequency distributions of these soil properties are displayed in the  
639 right corner. Dashed polygons represent the continental part of California. In the  
640 histograms, the blue and red dashed lines represent the mean and median values,  
641 respectively. The maps labeled D0 to D5 correspond to the first vertical layer down to  
642 the deepest layer. Note the map and distribution of soil organic matter (SOM) is log-  
643 scaled. Mean and median values are computed from the original SOM data.

Deleted: ,

Deleted: ,

644  
645 Soil profiles used for evaluating residual correction are grouped according to their  
646 corresponding pixel's land use classification from the National Land Cover Database  
647 (NLCD). Figure 8 presents selected vertical soil profiles of sand content, oven-dry bulk  
648 density, and SOM across three land use categories: forest, cultivated crops, and wetland.  
649 The number of samples varies by land use, with forests having the most, cultivated crops  
650 approximately half as many, and wetlands the fewest across California. To ensure a  
651 balanced visualization, a similar number of profiles are selected from each category. Sand  
652 content is chosen due to its broader range of variation (0-100%~~mass~~) compared to silt and  
653 clay (< 60% range). SOM and bulk density, which show relatively lower performance  
654 metrics, are included to assess the model's 'lower-bound performance'. These vertical  
655 profiles were not used during model training.

Deleted: %)

660 In Figure 8, solid lines represent the mean soil profiles for sand content, oven-dry bulk  
661 density, and SOM across forest, cultivated crops, and wetland land use categories. Blue  
662 lines, red lines, and green lines indicate prior, observation, and posterior predictions.  
663 Comparing the solid lines, the posterior predictions align more closely with the observed  
664 data compared to the prior estimates. However, the degree of alignment varies by soil  
665 property. For sand content and SOM, the posterior predictions show better agreement with  
666 observations, while bulk density predictions exhibit greater discrepancies, particularly in  
667 cultivated areas.

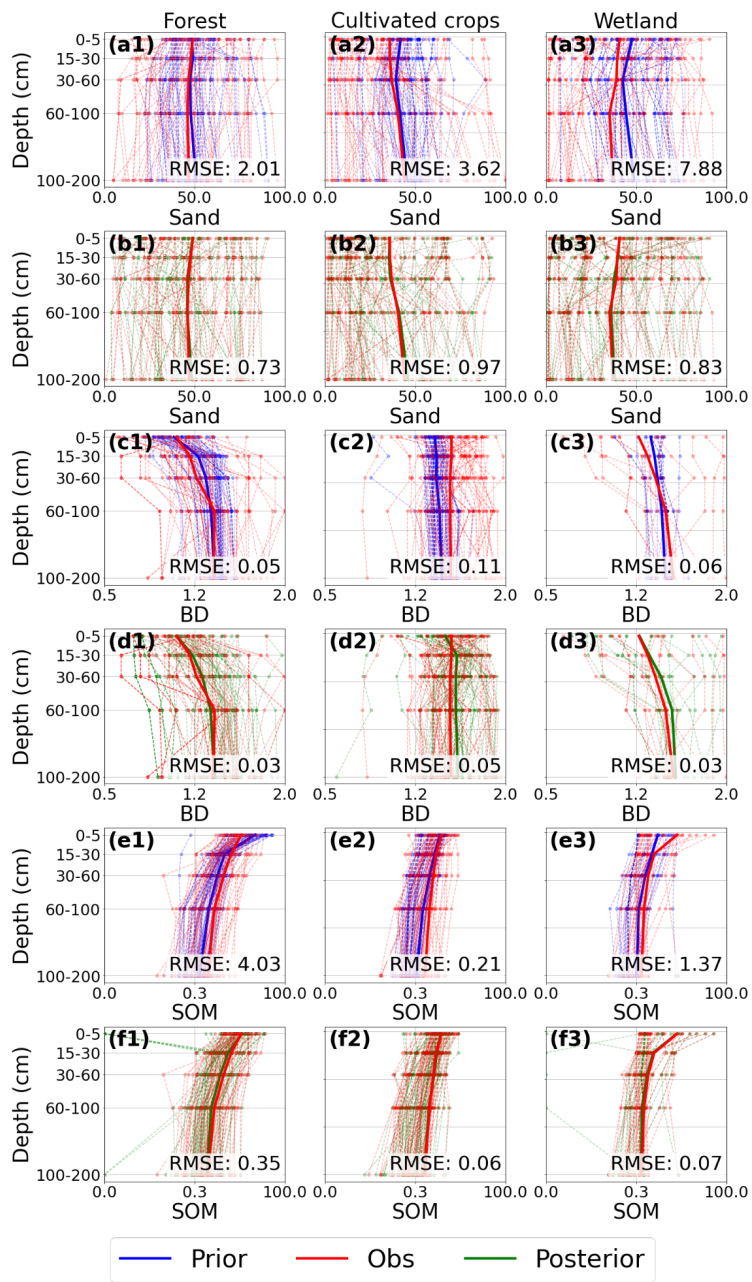
668  
669 For sand content, the residual correction process improves estimates, especially in  
670 wetlands, with RMSE decreasing from 7.68 to 0.77 (% mass). Bulk density predictions  
671 perform better in forested and wetland areas. In cultivated crops, the posterior predictions  
672 show larger discrepancies. This suggests that bulk density is more challenging to predict in  
673 agricultural lands, particularly in shallow layers, likely due to agricultural activities. For  
674 SOM, the residual correction effectively improves estimates, especially in the surface  
675 layers of wetlands.

676  
677 Dashed lines in Figure 8 represent individual soil profiles. Prior predictions often  
678 underestimated the variability in soil properties, struggling to capture extreme values. After  
679 the residual correction, the posterior predictions are better able to approximate these  
680 extremes. However, the correction process sometimes introduces additional noise. For  
681 example, some low SOM values were generated during residual correction, even though

Deleted: (%)

Deleted: (such as 0.001 g/cm<sup>3</sup>)

684 such values are not presented in the observed data. It is likely due to that we used the van  
685 Bemmelen factor (1.724) to convert the prior soil organic matter to soil organic carbon.



687 **Figure 8: Vertical distribution of soil properties (sand content, oven-dry bulk density**  
688 **BD, and soil organic matter SOM) across three land use categories: forest, cultivated**  
689 **crops, and wetland. Prior estimates (blue), posterior estimates (green), and**  
690 **observations (red) are shown as depth profiles. Dashed lines represent individual**  
691 **measurements, and solid lines show mean values. RMSE is computed elementwise to**  
692 **evaluate model performance across all depths. X-axis and Y-axis represent value**  
693 **ranges of a soil property and vertical depth intervals, respectively.**

694

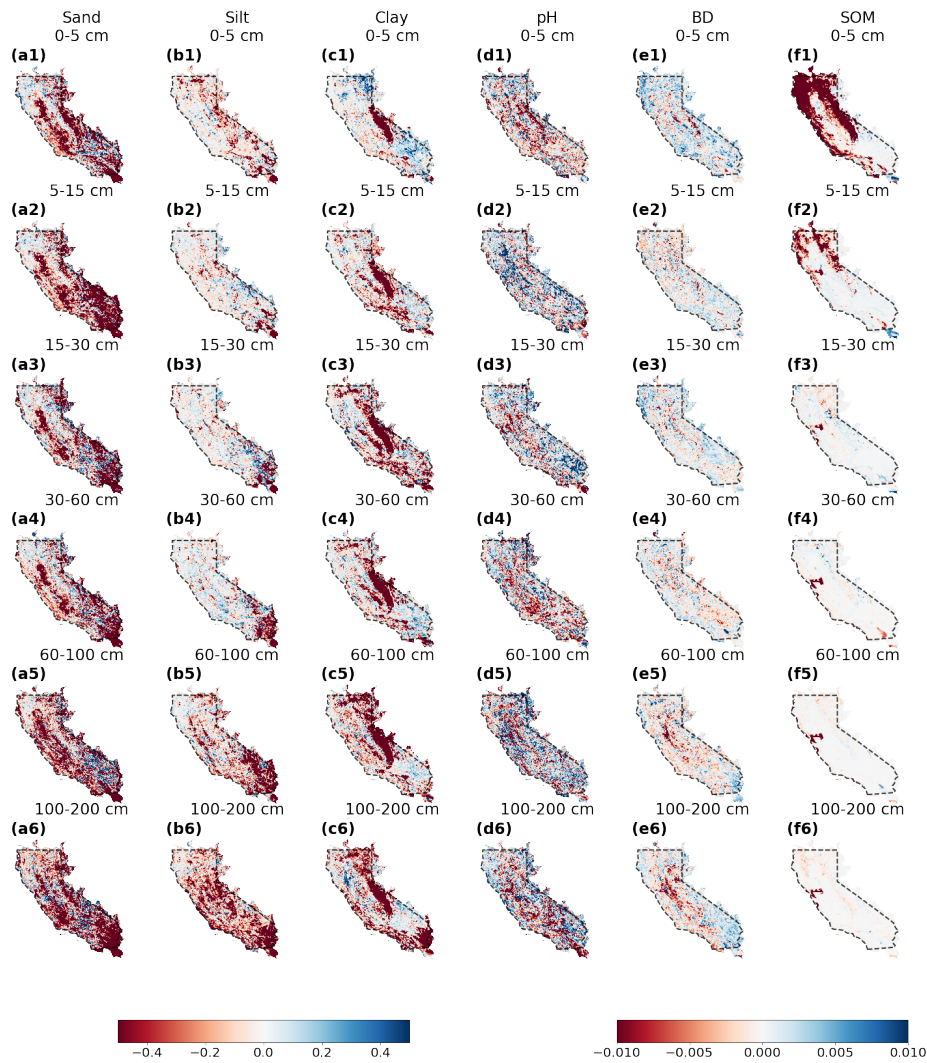
### 695 **3.3 Uncertainty Analysis**

696 Figure 9 shows the differences between 5% — 95% posterior and prior prediction interval  
697 widths (PIWs) for six soil properties—sand, silt, clay, pH, bulk density, and SOM—from  
698 surface to 2-m deep. The differences are calculated by subtracting the prior PIWs from the  
699 posteriors. Red areas present a reduction in posterior PIW, indicating the residual  
700 correction has reduced uncertainties of soil properties predictions. Blue pixels suggest the  
701 opposite. White areas represent regions where the prior and posterior uncertainties are  
702 similar.

703

704 In Figure 9, most pixels show reduced uncertainty for sand content after residual  
705 correction, particularly in agricultural and desert regions. This improvement is attributed to  
706 the inclusion of additional soil profile data from these areas. For clay content, the posterior  
707 predictions consistently show reduced uncertainty across the Sierra Nevada Mountain  
708 ranges. For SOM, the posterior PIWs improved in shallower layers (0-15 cm) over both the

709 Coastal Ranges and the Sierra Nevada Mountains, with the coastal line showing notably  
710 narrower PIWs. For pH, the results present a mixed pattern of PIWs after residual  
711 correction, with some areas showing reduced uncertainty and others showing the  
712 opposite. Similarly, bulk density exhibits a mixed pattern, though deeper layers (60 cm to 2  
713 m) generally show reduced uncertainty in the Central Valley, California.



714

715 **Figure 9: Differences of 5% — 95% posterior and prior prediction interval widths (PIWs)**

716 **for soil properties across different depths. Each column represents a specific soil**

717 **property and rows show different depths. Black polygons represent the continental**

718 **differences between posterior and prior PIWs are in a red-to-blue**

719 **color scale. Red pixels indicate a decrease in posterior PIW, indicating residual**  
720 **correction reduces uncertainties. Vice versa for blue pixels. White areas indicate**  
721 **similar extent of uncertainties. The left colorbar corresponds to sand, silt, clay with**  
722 **wider ranges of PIW differences. The right colorbar represents other properties with**  
723 **smaller PIW changes.**

724

## 725 **4 Discussion**

### 726 **4.1 Limitations in Soil Profile Data**

727 The effectiveness of residual correction depends on the spatial and vertical distribution of  
728 soil profiles used to calculate residuals. In regions with sparse sampling, such as  
729 California's desert areas (Figure 1), the limited number of profiles leads to interpolating the  
730 entire area using limited observations. If soil heterogeneity is not captured by these limited  
731 samples, the residual correction would overlook it. For soil texture, most data collected by  
732 staff working on multiple projects under the National Institute of Food and Agriculture  
733 (NIFA) and the Sustainable Agricultural Systems (SAS) programs range from the surface to  
734 1.1 meters deep (additional field measurements used in this work). We use spline  
735 interpolation to predict soil texture data beyond 1.1-m depths. It assumes vertical  
736 continuity in soil properties, which may not reflect abrupt changes in subsurface layers.

737

738 Uncertainty also arises from converting some soil organic carbon (SOC) data to soil  
739 organic matter (SOM). We used the van Bemmelen factor (1.724) to convert SOC to SOM  
740 profiles. This factor does not hold true in scenarios such as organic-rich soils. Adding data

741 quality controls—such as filtering profiles based on metadata (such as soil type, land  
742 use)—could filter out samples that are not suitable for this conversion. However, this  
743 conversion still has uncertainties, since even for mineral soils, this factor still has a certain  
744 extent of variation depending on the organic matter composition (lower for soils with more  
745 decomposed organic matter), soil types (forest soils or wetland soils with anaerobic  
746 decomposition), and environmental influences (such as microbial activity).

747

#### 748 **4.2 Computational Challenges**

749 The iterative residual correction process on distributions requires computational  
750 resources, particularly when applied to large-extent or high-resolution datasets. This  
751 process involves adjusting multiple values for each pixel, as each pixel represents a  
752 distribution of soil properties. This process can be approached in two ways. The first  
753 method involves correcting the residual values for each pixel, adding these residuals to  
754 update the posterior values of soil properties, and then converting these updated values to  
755 generate a posterior distribution of soil properties. The second method first converts all  
756 pixel values into the same histogram bins and then corrects the shape of these histogram  
757 bins for each pixel. Thus, the number of values retained per pixel affects computational  
758 expense. Based on our experience, using method two, especially for soil texture, requires  
759 100-bin histograms. Using method one with 20 most probable prior property values for  
760 residual correction can achieve comparable results while reducing memory usage.

761

762 The iterative process of updating features and correcting residuals also plays a role. In our  
763 simulations, we observed that subsequent residual corrections generally align with  
764 previous ones. To ensure consistency, we require the corrections to converge more than  
765 three times across different depths. For example, residual correction for a 1-km soil  
766 property map over California takes approximately two hours after preprocessing the input  
767 data. However, processing higher-resolution datasets, such as those at a 10-meter scale,  
768 can demand significantly more computational resources. This highlights the trade-off  
769 between resolution and computational efficiency in DSM projects.

770

#### 771 **4.3 Temporal and Spatial Constraints**

772 The current method does not account for temporal changes in soil properties, limiting its  
773 applicability to dynamic properties like soil organic matter or bulk density. Incorporating  
774 temporal covariates (such as seasonal land surface temperature, recent land-use  
775 changes) or stratifying soil profiles by collection date could address this. However, such  
776 improvements rely on the availability of temporally resolved soil data, which are often  
777 limited in quantities and sampling frequency.

778

779 Spatial clustering of soil samples poses another challenge. While duplicate profiles were  
780 removed during data preprocessing, nearby samples may still share a certain level of  
781 similarity due to spatial autocorrelation. This could lead to overly optimistic evaluation of  
782 residual correction performance. Two methods can help address this issue:

783 (1) Cross-validation with spatial considerations: Implement a cross-validation  
784 method for splitting training and validation sets with attention to sample locations.  
785 Ensure a minimum distance between training samples and evaluation data.

786  
787 (2) Independent dataset evaluation: Use independent datasets to evaluate the  
788 model. CONUS-wide instrumental network, such as the U.S. Climate Reference  
789 Network and the National Ecological Observatory Network, provide independent  
790 soil data. However, these datasets have limitations as they were collected with  
791 clustering to certain landscapes, potentially introducing bias in the evaluation.

792

#### 793 **4.4 Similar Studies**

794 Several continental-scale DSM products (or methods) are compared, including the Soil  
795 Survey Geographic Database (SSURGO), the Gridded National Soil Survey Geographic  
796 Database (gNATSGO), the Probabilistic Layers for the Assessment of Soils (POLARIS), Soil-  
797 Landscape Unified Synthesis (SOLUS), and the pruned Hierarchical Random Forest with  
798 iterative bias correction (pHRF with IRC) soil properties. SSURGO is a traditional, polygon-  
799 based product derived from expert field surveys and remains widely used in agricultural  
800 applications (Soil Survey Staff et al., 2023). gNATSGO mainly builds on SSURGO by  
801 rasterizing its map units to improve spatial coverage. And its estimation of soil properties  
802 still rely on utilizing metadata of legacy soil data (Soil survey staff, 2023). These two still  
803 inherit legacy data's limitations, such as scale inconsistency between soil map units and  
804 derived soil maps, inconsistencies with field observations, and report distribution of soil

805 properties with only three values (low end value, representative value, and high end value)  
806 (Rossiter et al., 2022; Soil Survey Staff, 2025; Xu et al., 2025).

807  
808 Development of the following DSM products incorporates quantitative models in their  
809 methodology. POLARIS produces probabilistic soil property maps using machine learning  
810 and the DSMART algorithm (Chaney et al., 2016, 2019; Odgers et al., 2015), while the  
811 uncertainties in the DSMART algorithm can propagate into POLARIS. SOLUS integrates  
812 legacy soil data with georeferenced field observations and employs linear adjusted  
813 Random Forest to predict soil properties (Nauman et al., 2024). SOLUS hierarchizes soil  
814 data with different qualities into its training dataset, giving more attention to georeferenced  
815 observations. However, since it also uses resampled soil data derived from polygon-based  
816 soil map units, this process may introduce additional uncertainties into the final product.  
817 The pHRF with IRC follows a different approach. Unlike most DSM methods that directly  
818 predict soil properties from input data, this approach works in two steps: first, it generates  
819 a prior estimate of soil taxa and property values, then iteratively adjusts these estimates to  
820 improve model performance. In future work, the pHRF with IRC method will be applied on  
821 large scale and assessed with more soil properties to evaluate its generalizability.

822

## 823 **5 Conclusion**

824 The study introduces an iterative residual correction method for post processing used in a  
825 Digital Soil Mapping (DSM) framework. The method integrates additional soil profile data  
826 and iteratively optimizes the feature space to refine the distribution of soil properties until

827 the residual correction model converges. Convergence is achieved when the median  
828 difference between updated and previous predictions falls below a predefined threshold,  
829 ensuring consistent predictions. The proposed DSM method operates through two primary  
830 steps: (1) generating prior soil property maps using the pruned hierarchical Random Forest  
831 (pHRF) approach, and (2) performing iterative residual correction on the priors. Residuals  
832 (differences between observed values and prior predictions) are calculated and added to  
833 the prior values of soil property to adjust the statistical shape of the probability distribution  
834 pixel-by-pixel. The feature space, which includes soil covariates, depth information, and  
835 vertical correlations, is iteratively optimized to capture incremental adjustments to  
836 subsequent predictions.

837

838 Using this method, we updated posterior distribution of soil properties for sand, silt, clay  
839 content, soil pH, oven-dry bulk density, and soil organic matter over California. The results  
840 show improvements in the accuracy of soil properties predictions, as shown by multiple  
841 metrics including RMSE,  $R^2$ , and correlation coefficients. Furthermore, the iterative  
842 residual correction model reduced prediction uncertainties, presenting narrower  
843 prediction intervals compared to the priors.

844

845 Several innovations contribute to the method's improvements. First, the integration of  
846 additional soil profiles allows the model to further learn from georeferenced soil  
847 information, complementing prior soil property estimates derived from traditional  
848 surveys. Second, the iterative update of feature space captures both spatial and vertical

849 soil heterogeneity through a carefully selected combination of soil covariates and vertical  
850 correlations among soil profile observations. Third, the convergence-based approach to  
851 residual correction ensures stable output of posterior predictions while avoiding overfitting  
852 since only converged residuals are added to the priors. Fourth, the implementation of  
853 physical constraints and compositional data handling maintains the realism of predicted  
854 soil properties. Future research could explore the application of this framework to other  
855 soil properties and environmental contexts, such as soil hydraulic properties and CONUS-  
856 wide simulation, to test the framework's generalization, supporting informed decision-  
857 making in soil-related applications.

858

#### 859 **Data Availability**

860 Data will be made available on request. Code is available on  
861 [https://github.com/emmaxu43/IRC\\_CA/tree/main](https://github.com/emmaxu43/IRC_CA/tree/main).

862

#### 863 **Author Contributions**

864 Chengcheng Xu and Nathaniel Chaney designed the study and developed the  
865 methodology. Chengcheng Xu wrote the original draft and wrote the codes to produce the  
866 methodology and analyses. Nathaniel Chaney supervised the work, provided resources  
867 and funding, and helped guide the research direction. Elia Scudiero provided funding,  
868 project management, co-supervision. Elia Scudiero and Ray Anderson provided soil  
869 property samples from California that were used as part of the input dataset. Chengcheng

870 Xu, Nathaniel Chaney, Elia Scudiero, and Ray Anderson discussed the results and  
871 contributed to revising and editing the manuscript.

872

873 **Competing Interests**

874 The authors declare that they have no conflict of interest.

875

876 **Acknowledgements**

877 This research was supported by the Agriculture and Food Research Initiative Competitive  
878 Grant no. 2020-69012-31914 from the USDA National Institute of Food and Agriculture. The  
879 authors want to thank Dr. Todd Skaggs for his and his teams' support for gathering input  
880 data for this work. His and Dr. Ray Anderson's efforts are supported by USDA-ARS, Office  
881 of National Programs (projects 2036-61000-019-000-D and 2036-61000-019-006-R). The  
882 U.S. Department of Agriculture prohibits discrimination in all its programs and activities on  
883 the basis of race, color, national origin, age, disability, and where applicable, sex, marital  
884 status, familial status, parental status, religion, sexual orientation, genetic information,  
885 political beliefs, reprisal, or because all or part of an individual's income is derived from  
886 any public assistance program (not all prohibited bases apply to all programs). Persons  
887 with disabilities who require alternative means for communication of program information  
888 (braille, large print, audiotape, etc.) should contact USDA's TARGET Center at (202) 720-  
889 2600 (voice and TDD). To file a complaint of discrimination, write to USDA, Director, Office  
890 of Civil Rights, 1400 Independence Avenue, S.W., Washington, D.C. 20250-9410, or call

891 (800) 795-3272 (voice) or (202) 720-6382 (TDD). USDA is an equal opportunity provider and  
892 employer.

893

#### 894 **Financial Support**

895 The study was supported by USDA-NIFA-AFRI-006739 grant for sustainable agricultural  
896 systems.

897

#### 898 **References**

- 899 Arrouays, D., McKenzie, N., Hempel, J., Forges, A. R. de, and McBratney, A. B.:  
900 GlobalSoilMap: Basis of the global spatial soil information system, CRC Press, 496 pp.,  
901 2014.
- 902 Batjes, N. H., Calisto, L., and de Sousa, L. M.: Providing quality-assessed and standardised  
903 soil data to support global mapping and modelling (WoSIS snapshot 2023), *Earth System*  
904 *Science Data*, 16, 4735–4765, <https://doi.org/10.5194/essd-16-4735-2024>, 2024.
- 905 Chaney, N. W., Wood, E. F., McBratney, A. B., Hempel, J. W., Nauman, T. W., Brungard, C.  
906 W., and Odgers, N. P.: POLARIS: A 30-meter probabilistic soil series map of the contiguous  
907 United States, *Geoderma*, <https://doi.org/10.1016/j.geoderma.2016.03.025>, 2016.
- 908 Chaney, N. W., Minasny, B., Herman, J. D., Nauman, T. W., Brungard, C. W., Morgan, C. L.  
909 S., McBratney, A. B., Wood, E. F., and Yimam, Y.: POLARIS Soil Properties: 30-m  
910 Probabilistic Maps of Soil Properties Over the Contiguous United States, *Water Resources*  
911 *Research*, <https://doi.org/10.1029/2018WR022797>, 2019.
- 912 Chen, C., Liaw, A., and Breiman, L.: Using random forest to learn imbalanced data,  
913 *University of California, Berkeley*, 110, 24, 2004.
- 914 Chilès, J.-P. and Delfiner, P.: Geostatistics: modeling spatial uncertainty, in: *Geostatistics:*  
915 *modeling spatial uncertainty*, John Wiley & Sons, Ltd, 147–237,  
916 <https://doi.org/10.1002/9781118136188.ch3>, 2012.
- 917 Corwin, D. L. and Scudiero, E.: Field-scale apparent soil electrical conductivity, *Soil*  
918 *Science Society of America Journal*, 84, 1405–1441, <https://doi.org/10.1002/saj2.20153>,  
919 2020.

- 920 Grunwald, S., Thompson, J. A., and Boettinger, J. L.: Digital Soil Mapping and Modeling at  
921 Continental Scales: Finding Solutions for Global Issues, *Soil Science Society of America*  
922 *Journal*, 75, 1201–1213, <https://doi.org/10.2136/SSSAJ2011.0025>, 2011.
- 923 Haghverdi, A., Najarchi, M., öztürk, H. S., and Durner, W.: Studying unimodal, bimodal, PDI  
924 and bimodal-PDI variants of multiple soil water retention models: I. Direct model fit using  
925 the extended evaporation and dewpoint methods, *Water (Switzerland)*, 12,  
926 <https://doi.org/10.3390/w12030900>, 2020.
- 927 Hartemink, A. E., Hempel, J., Lagacherie, P., McBratney, A., McKenzie, N., MacMillan, R. A.,  
928 Minasny, B., Montanarella, L., de Mendonça Santos, M. L., Sanchez, P., Walsh, M., and  
929 Zhang, G.-L.: GlobalSoilMap.net – A New Digital Soil Map of the World, in: *Digital Soil*  
930 *Mapping: Bridging Research, Environmental Application, and Operation*, edited by:  
931 Boettinger, J. L., Howell, D. W., Moore, A. C., Hartemink, A. E., and Kienast-Brown, S.,  
932 Springer Netherlands, Dordrecht, 423–428, [https://doi.org/10.1007/978-90-481-8863-](https://doi.org/10.1007/978-90-481-8863-5_33)  
933 [5\\_33](https://doi.org/10.1007/978-90-481-8863-5_33), 2010.
- 934 Hengl, T., Heuvelink, G. B., and Stein, A.: A generic framework for spatial prediction of soil  
935 variables based on regression-kriging, *Geoderma*, 120, 75–93, 2004.
- 936 Hengl, T., De Jesus, J. M., Heuvelink, G. B. M., Gonzalez, M. R., Kilibarda, M., Blagotić, A.,  
937 Shangguan, W., Wright, M. N., Geng, X., Bauer-Marschallinger, B., Guevara, M. A., Vargas,  
938 R., MacMillan, R. A., Batjes, N. H., Leenaars, J. G. B., Ribeiro, E., Wheeler, I., Mantel, S.,  
939 and Kempen, B.: SoilGrids250m: Global gridded soil information based on machine  
940 learning, *PLoS ONE*, <https://doi.org/10.1371/journal.pone.0169748>, 2017.
- 941 Jiang, Q., Fu, Q., and Wang, Z.: Delineating site-specific irrigation management zones,  
942 *Irrigation and Drainage*, 60, 464–472, <https://doi.org/10.1002/ird.588>, 2011.
- 943 Lesch, S., Rhoades, J., and Corwin, D.: ESAP-95 version 2.01 R: User manual and tutorial  
944 guide, *Research Rpt*, 146, 17, 2000.
- 945 Lesch, S. M.: Sensor-directed response surface sampling designs for characterizing spatial  
946 variation in soil properties, *Computers and Electronics in Agriculture*, 46, 153–179,  
947 <https://doi.org/10.1016/j.compag.2004.11.004>, 2005.
- 948 Li, N., Zhao, X., Wang, J., Sefton, M., and Triantafyllis, J.: Digital soil mapping based site-  
949 specific nutrient management in a sugarcane field in Burdekin, *Geoderma*, 340, 38–48,  
950 <https://doi.org/10.1016/j.geoderma.2018.12.033>, 2019.
- 951 McBratney, A. B., Mendonça Santos, M. L., and Minasny, B.: On digital soil mapping,  
952 *Geoderma*, 117, 3–52, [https://doi.org/10.1016/S0016-7061\(03\)00223-4](https://doi.org/10.1016/S0016-7061(03)00223-4), 2003.
- 953 Minasny, B. and McBratney, A. B.: A conditioned Latin hypercube method for sampling in  
954 the presence of ancillary information, *Computers & geosciences*, 32, 1378–1388, 2006.

955 Mueller, T. G., Pierce, F. J., Schabenberger, O., and Warncke, D. D.: Map Quality for Site-  
956 Specific Fertility Management, *Soil Science Society of America Journal*, 65, 1547–1558,  
957 <https://doi.org/10.2136/sssaj2001.6551547x>, 2001.

958 National Cooperative Soil Survey: NCSS Soil Characterization Database (Lab Data Mart),  
959 2018.

960 Nauman, T. W., Kienast-Brown, S., Roecker, S. M., Brungard, C., White, D., Philippe, J., and  
961 Thompson, J. A.: Soil landscapes of the United States (SOLUS): Developing predictive soil  
962 property maps of the conterminous United States using hybrid training sets, *Soil Science  
963 Society of America Journal*, 88, 2046–2065, <https://doi.org/10.1002/saj2.20769>, 2024.

964 Nussbaum, M., Zimmermann, S., Walther, L., and Baltensweiler, A.: Benefits of  
965 hierarchical predictions for digital soil mapping—An approach to map bimodal soil pH,  
966 *Geoderma*, 437, 116579, <https://doi.org/10.1016/j.geoderma.2023.116579>, 2023.

967 Odgers, N. P., McBratney, A. B., and Minasny, B.: Digital soil property mapping and  
968 uncertainty estimation using soil class probability rasters, *Geoderma*, 237,  
969 <https://doi.org/10.1016/j.geoderma.2014.09.009>, 2015.

970 Oliver, M. A. and Webster, R.: A tutorial guide to geostatistics: Computing and modelling  
971 variograms and kriging, *CATENA*, 113, 56–69,  
972 <https://doi.org/10.1016/j.catena.2013.09.006>, 2014.

973 Ortuani, B., Chiaradia, E. A., Priori, S., L'Abate, G., Canone, D., Comunian, A., Giudici, M.,  
974 Mele, M., and Facchi, A.: Mapping Soil Water Capacity Through EMI Survey to Delineate  
975 Site-Specific Management Units Within an Irrigated Field, *Soil Science*, 181, 252,  
976 <https://doi.org/10.1097/SS.000000000000159>, 2016.

977 Poggio, L., De Sousa, L. M., Batjes, N. H., Heuvelink, G. B. M., Kempen, B., Ribeiro, E., and  
978 Rossiter, D.: SoilGrids 2.0: Producing soil information for the globe with quantified spatial  
979 uncertainty, *SOIL*, 7, 217–240, <https://doi.org/10.5194/SOIL-7-217-2021>, 2021.

980 Powers, J. S., Corre, M. D., Twine, T. E., and Veldkamp, E.: Geographic bias of field  
981 observations of soil carbon stocks with tropical land-use changes precludes spatial  
982 extrapolation, *Proceedings of the National Academy of Sciences*, 108, 6318–6322,  
983 <https://doi.org/10.1073/pnas.1016774108>, 2011.

984 Ramcharan, A., Hengl, T., Nauman, T., Brungard, C., Waltman, S., Wills, S., and Thompson,  
985 J.: Soil Property and Class Maps of the Conterminous United States at 100-Meter Spatial  
986 Resolution, *Soil Science Society of America Journal*, 82, 186–201,  
987 <https://doi.org/10.2136/sssaj2017.04.0122>, 2018.

988 Rossiter, D. G., Poggio, L., Beaudette, D., and Libohova, Z.: How well does digital soil  
989 mapping represent soil geography? An investigation from the USA, *SOIL*, 8, 559–586,  
990 <https://doi.org/10.5194/soil-8-559-2022>, 2022.

- 991 Schmidinger, J. and Heuvelink, G. B. M.: Validation of uncertainty predictions in digital soil  
 992 mapping, *Geoderma*, 437, 116585, <https://doi.org/10.1016/j.geoderma.2023.116585>,  
 993 2023.
- 994 Scudiero, E., Corwin, D. L., Markley, P. T., Pourreza, A., Rounsaville, T., Bughici, T., and  
 995 Skaggs, T. H.: A system for concurrent on-the-go soil apparent electrical conductivity and  
 996 gamma-ray sensing in micro-irrigated orchards, *Soil and Tillage Research*, 235, 105899,  
 997 2024.
- 998 Sharififar, A., Sarmadian, F., Malone, B. P., and Minasny, B.: Addressing the issue of digital  
 999 mapping of soil classes with imbalanced class observations, *Geoderma*, 350, 84–92,  
 1000 <https://doi.org/10.1016/j.geoderma.2019.05.016>, 2019.
- 1001 Shi, G., Sun, W., Shangguan, W., Wei, Z., Yuan, H., Zhang, Y., Liang, H., Li, L., Sun, X., Li, D.,  
 1002 Huang, F., Li, Q., and Dai, Y.: A China dataset of soil properties for land surface modeling  
 1003 (version 2), <https://doi.org/10.5194/essd-2024-299>, 29 August 2024.
- 1004 Soil, K.: Survey laboratory methods manual, Soil Survey Investigations Report, 1996.
- 1005 Soil Survey Staff: Kellogg Soil Survey Laboratory methods manual, U.S. Department of  
 1006 Agriculture, Natural Resources Conservation Service, Lincoln, Nebraska, 2014.
- 1007 Soil survey staff: Gridded National Soil Survey Geographic (gNATSGO) Database for the  
 1008 Conterminous United States, 2023. Natural Resources Conservation Service, United  
 1009 States Department of Agriculture.
- 1010 Soil Survey Staff: Gridded Soil Survey Geographic (gSSURGO) Database for the  
 1011 Conterminous United States, 2025. Natural Resources Conservation Service, United  
 1012 States Department of Agriculture.
- 1013 Soil Survey Staff, Natural Resources Conservation Service, and United States Department  
 1014 of Agriculture: Soil Survey Geographic (SSURGO) Database for the CONUS, 2023. Natural  
 1015 Resources Conservation Service, United States Department of Agriculture.
- 1016 Sylvain, J.-D., Anctil, F., and Thiffault, É.: Using bias correction and ensemble modelling for  
 1017 predictive mapping and related uncertainty: A case study in digital soil mapping,  
 1018 *Geoderma*, 403, 115153, <https://doi.org/10.1016/j.geoderma.2021.115153>, 2021.
- 1019 Takoutsing, B., Heuvelink, G. B. M., Stoorvogel, J. J., Shepherd, K. D., and Aynekulu, E.:  
 1020 Accounting for analytical and proximal soil sensing errors in digital soil mapping, *European  
 1021 Journal of Soil Science*, 73, e13226, <https://doi.org/10.1111/ejss.13226>, 2022.
- 1022 Vereecken, H., Schnepf, A., Hopmans, J. W., Javaux, M., Or, D., Roose, T., Vanderborght, J.,  
 1023 Young, M. H., Amelung, W., Aitkenhead, M., Allison, S. D., Assouline, S., Baveye, P., Berli,  
 1024 M., Brüggemann, N., Finke, P., Flury, M., Gaiser, T., Govers, G., Ghezzehei, T., Hallett, P.,  
 1025 Hendricks Franssen, H. J., Heppell, J., Horn, R., Huisman, J. A., Jacques, D., Jonard, F.,

- 1026 Kollet, S., Lafolie, F., Lamorski, K., Leitner, D., McBratney, A., Minasny, B., Montzka, C.,  
1027 Nowak, W., Pachepsky, Y., Padarian, J., Romano, N., Roth, K., Rothfuss, Y., Rowe, E. C.,  
1028 Schwen, A., Šimůnek, J., Tiktak, A., Van Dam, J., van der Zee, S. E. A. T. M., Vogel, H. J.,  
1029 Vrugt, J. A., Wöhling, T., and Young, I. M.: Modeling Soil Processes: Review, Key  
1030 Challenges, and New Perspectives, *Vadose Zone Journal*, 15, vzt2015.09.0131,  
1031 <https://doi.org/10.2136/vzj2015.09.0131>, 2016.
- 1032 Vereecken, H., Amelung, W., Bauke, S. L., Bogaen, H., Brüggemann, N., Montzka, C.,  
1033 Vanderborght, J., Bechtold, M., Blöschl, G., Carminati, A., Javaux, M., Konings, A. G.,  
1034 Kusche, J., Neuweiler, I., Or, D., Steele-Dunne, S., Verhoef, A., Young, M., and Zhang, Y.:  
1035 Soil hydrology in the Earth system, *Nat Rev Earth Environ*, 3, 573–587,  
1036 <https://doi.org/10.1038/s43017-022-00324-6>, 2022.
- 1037 Wu, Y., Huang, Y., Chen, Z., Yao, Z., Fu, Y., Liu, K., Luo, X., and Wang, D.: Iterative Feature  
1038 Space Optimization through Incremental Adaptive Evaluation,  
1039 <https://doi.org/10.48550/arXiv.2501.14889>, 24 January 2025.
- 1040 Xu, C., Huang, J., Hartemink, A. E., and Chaney, N. W.: Pruned hierarchical Random Forest  
1041 framework for digital soil mapping: Evaluation using NEON soil properties, *Geoderma*, 459,  
1042 117392, <https://doi.org/10.1016/j.geoderma.2025.117392>, 2025.
- 1043 Zhang, G. and Lu, Y.: Bias-corrected random forests in regression, *Journal of Applied*  
1044 *Statistics*, 39, 151–160, <https://doi.org/10.1080/02664763.2011.578621>, 2012.
- 1045